INTERNATIONAL JOURNAL FOR NUMERICAL METHODS IN ENGINEERING
*Int. J. Numer. Meth. Engng* 2009; **78**:324–353
Published online 18 November 2008 in Wiley InterScience (www.interscience.wiley.com). DOI: 10.1002/nme.2491

# A face-based smoothed finite element method (FS-FEM) for 3D linear and geometrically non-linear solid mechanics problems using 4-node tetrahedral elements

T. Nguyen-Thoi[1,*,†], G. R. Liu[1,2], K. Y. Lam[3] and G. Y. Zhang[1,2]

[1]*Center for Advanced Computations in Engineering Science (ACES), Department of Mechanical Engineering, National University of Singapore, 9 Engineering Drive 1, Singapore 117576, Singapore*
[2]*Singapore-MIT Alliance (SMA), E4-04-10, 4 Engineering Drive 3, Singapore 117576, Singapore*
[3]*School of Mechanical and Aerospace Engineering, Nanyang Technological University, 50 Nanyang Avenue, Singapore 639798, Singapore*

SUMMARY

This paper presents a novel face-based smoothed finite element method (FS-FEM) to improve the accuracy of the finite element method (FEM) for three-dimensional (3D) problems. The FS-FEM uses 4-node tetrahedral elements that can be generated automatically for complicated domains. In the FS-FEM, the system stiffness matrix is computed using strains smoothed over the smoothing domains associated with the faces of the tetrahedral elements. The results demonstrated that the FS-FEM is significantly more accurate than the FEM using tetrahedral elements for both linear and geometrically non-linear solid mechanics problems. In addition, a novel domain-based selective scheme is proposed leading to a combined FS/NS-FEM model that is immune from volumetric locking and hence works well for nearly incompressible materials. The implementation of the FS-FEM is straightforward and no penalty parameters or additional degrees of freedom are used. The computational efficiency of the FS-FEM is found better than that of the FEM. 

Received 28 May 2008; Revised 24 September 2008; Accepted 24 September 2008

KEY WORDS: numerical methods; meshfree methods; tetrahedral elements; smoothed technique; finite element method (FEM); smoothed finite element method (SFEM); face-based smoothed finite element method (FS-FEM)

## 1. INTRODUCTION

The 4-node tetrahedral (T4) element is often used to introduce the procedures of the finite element method (FEM) in three dimensions (3D). The reason is that the T4 element can be very easily

*Correspondence to: T. Nguyen-Thoi, Center for Advanced Computations in Engineering Science (ACES), Department of Mechanical Engineering, National University of Singapore, 9 Engineering Drive 1, Singapore 117576, Singapore.
†E-mail: g0500347@nus.edu.sg

formulated and implemented using piecewise linear approximation. Furthermore, most FEM codes for adaptive analyses of 3D problems use tetrahedral elements, due to the simple fact that tetrahedral meshes can be automatically generated and refined, even for complicated domains.

However, T4 element of FEM also possesses significant shortcomings for problems of solid mechanics. Two such shortcomings are the well-known overly stiff behavior and volumetric locking in the nearly incompressible cases. In order to overcome these disadvantages, some new finite elements were proposed. Dohrmann *et al*. [1] presented a weighted least-squares approach in which a linear displacement field is fitted to an element's nodal displacements. The method is claimed to be computationally efficient and avoids the volumetric locking problems. However, more nodes are required on the element boundary to define the linear displacement field. Dohrmann *et al*. [2] also proposed a nodal integration FEM in which each element is associated with a single node and the linear interpolation functions of the original mesh are used. The method avoids the volumetric locking problems and performs better comparing with T4 element in terms of stress solution for static problems. However, for dynamic problems, the method is not stable due to the appearance of spurious modes at higher energy levels. Therefore, a stabilization scheme such as the one proposed by Puso and Solberg [3] is required for dynamic problems.

In the other front of development, meshfree methods have been developed for various types of problems [4, 5]. A strain-smoothing technique has been used by Chen *et al.* [6] to stabilize the nodal-integrated meshfree method and the natural-element method [7]. Liu [8] has applied this technique and extended it to a generalized gradient smoothing technique allowing the use of discontinuous functions. The generalized gradient smoothing technique offers a theoretical foundation to the so-called weakened weak formulation [9] for a wide class of compatible and incompatible methods, including the linear conforming point interpolation method (LC-PIM) [10, 11] and the linearly conforming radial point interpolation method [12] that use incompatible shape functions. Applying the same idea to the FEM, an element-based smoothed FEM (SFEM) [13–15] and a node-based

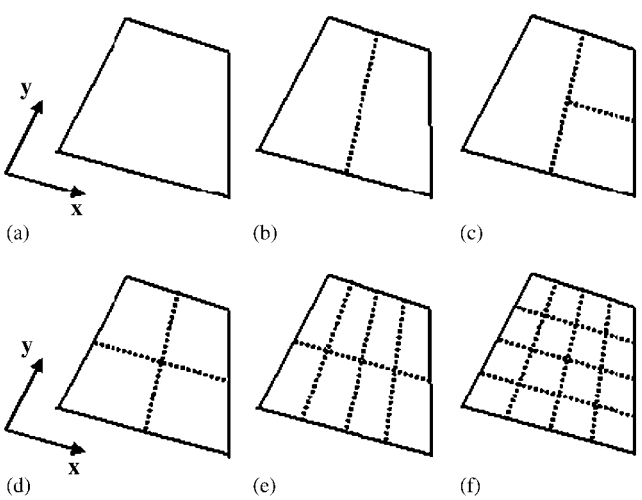


Figure 1. Division of quadrilateral element into the smoothing cells (SC) in the SFEM: (a) SC = 1; (b) SC = 2; (c) SC = 3; (d) SC = 4; (e) SC = 8; and (f) SC = 16.



DOI: 10.1002/nme

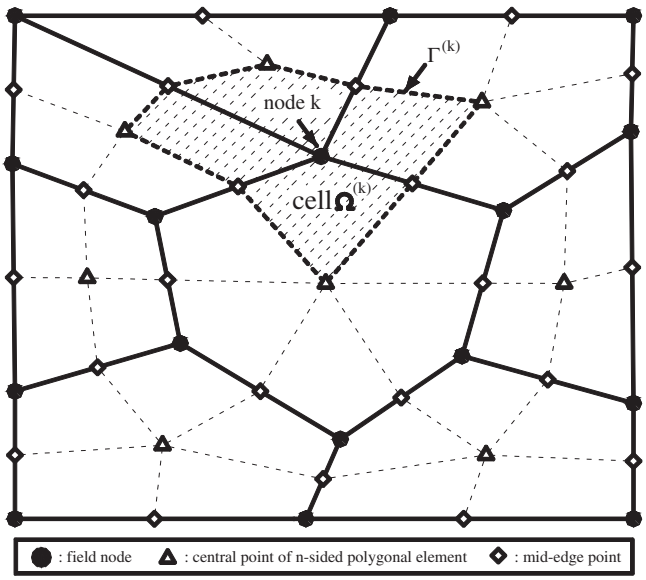


Figure 2. *n*-sided polygonal elements and the smoothing cell (shaded area) associated with nodes in the NS-FEM.

smoothed FEM (NS-FEM) [16] have also been formulated. In the SFEM, the strain-smoothing domains and the integration are performed over the quadrilateral elements, and these smoothing domains can be divided into one or many smoothing cells on each element, as shown in Figure 1. The SFEM has been developed for general *n*-sided polygonal elements [17], and further extended for plate and shell analyses [18, 19]. In the NS-FEM, the strain-smoothing domains and the integration are performed over the cells associated with nodes, and methods can be applied easily to triangular, 4-node quadrilateral, *n*-sided polygonal elements for 2D problems and tetrahedral elements for 3D problems. For *n*-sided polygonal elements, the cell $\Omega^{(k)}$ associated with the node $k$ is created by connecting sequentially the mid-edge-point to the central points of the surrounding *n*-sided polygonal elements of the node $k$ as shown in Figure 2. When only linear triangular or tetrahedral elements are used, the NS-FEM produces the same results as the method proposed by Dohrmann *et al.* [2] or the LC-PIM [12] using linear interpolation. Liu and Zhang [20] have provided an intuitive explanation and showed numerically that the LC-PIM can produce a upper bound to the exact solution in the strain energy, when a reasonably fine mesh is used. The upper bound property was also found in the NS-FEM [16]. Both upper and lower bounds in the strain energy for elastic solid mechanics problems can now be obtained by combining the NS-FEM with the SFEM (for *n*-sided polygonal elements) or with the FEM (for triangular or 4-node quadrilateral elements). Further developed, a nearly exact solution in strain energy using triangular and tetrahedral elements is also proposed by Liu *et al.* [21] by combining a scale factor $\alpha \in [0, 1]$ with the NS-FEM and the FEM to give a so-called the alpha Finite Element Method ($\alpha$FEM). Other idea was proposed by Duarte *et al.* [22] by combining $C^0$ Lagrange FE shape functions with the proposed $C^k$ partition of unity to give a so-called arbitrary smooth generalized finite element approximation ($C^k$ GFEM).

Recently, an edge-based smoothed FEM (ES-FEM) [23] was also formulated for static, free and forced vibration analyses in 2D problems. The ES-FEM uses triangular elements that can



DOI: 10.1002/nme

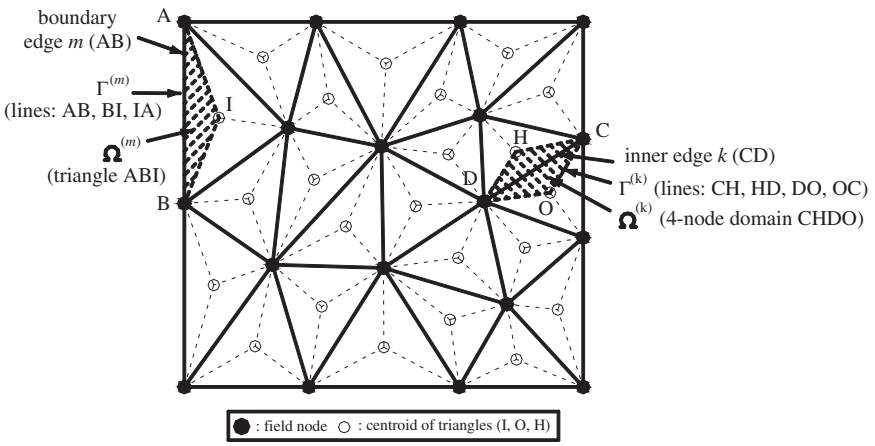


Figure 3. Triangular elements and the smoothing domains (shaded areas) associated with edges in the ES-FEM.

be generated automatically for complicated domains. In the ES-FEM, the system stiffness matrix is computed using strains smoothed over the smoothing domains associated with the edges of the triangles. For triangular elements, the smoothing domain $\Omega^{(k)}$ associated with the edge $k$ is created by connecting two endpoints of the edge to the two centroids of the two adjacent elements as shown in Figure 3. Extending the smoothing domain $\Omega^{(k)}$ associated with the edge $k$ to the quadrilateral or $n$-sided polygonal elements [24] is straightforward as shown in Figure 4.

The results demonstrated that the ES-FEM possesses the following excellent properties: (1) the ES-FEM model possesses a close-to-exact stiffness: it is much softer than the 'overly stiff' FEM and much stiffer than the 'overly soft' NS-FEM model; (2) the results are often found to be superconvergent and ultra-accurate: much more accurate than the linear triangular elements of FEM and even more accurate than those of the FEM using quadrilateral elements with the same sets of nodes; (3) there are no spurious non-zero energy modes found and hence the method is also stable and works well for vibration analysis; (4) the implementation of the method is straightforward and no penalty parameter is used, and the computational efficiency is better than the FEM using the same sets of nodes. In addition, a novel domain-based selective scheme is proposed leading to a combined ES/NS-FEM model that is immune from volumetric locking and hence works very well for nearly incompressible materials. These properties of the ES-FEM are confirmed using examples of static, free and forced vibration analyses of solids [23].

In this paper, we extend the idea of the ES-FEM for 3D problems. Instead of using the edges of the elements in 2D problems, we will use the faces of the elements as the base for smoothing domain construction for 3D problems. It is therefore termed as the face-based smoothed finite element method (FS-FEM). The FS-FEM uses T4 elements that can be generated automatically for complicated domains. In the FS-FEM, the system stiffness matrix is computed using strains smoothed over the smoothing domains associated with the faces of the tetrahedral elements, and hence is softer than that of T4 element. The results demonstrated that the FS-FEM is significantly more accurate than T4 element for both linear and geometrically non-linear problems. In addition, a novel domain-based selective scheme is proposed leading to a combined FS/NS-FEM model that is immune from volumetric locking and hence works well for nearly incompressible materials. The



DOI: 10.1002/nme

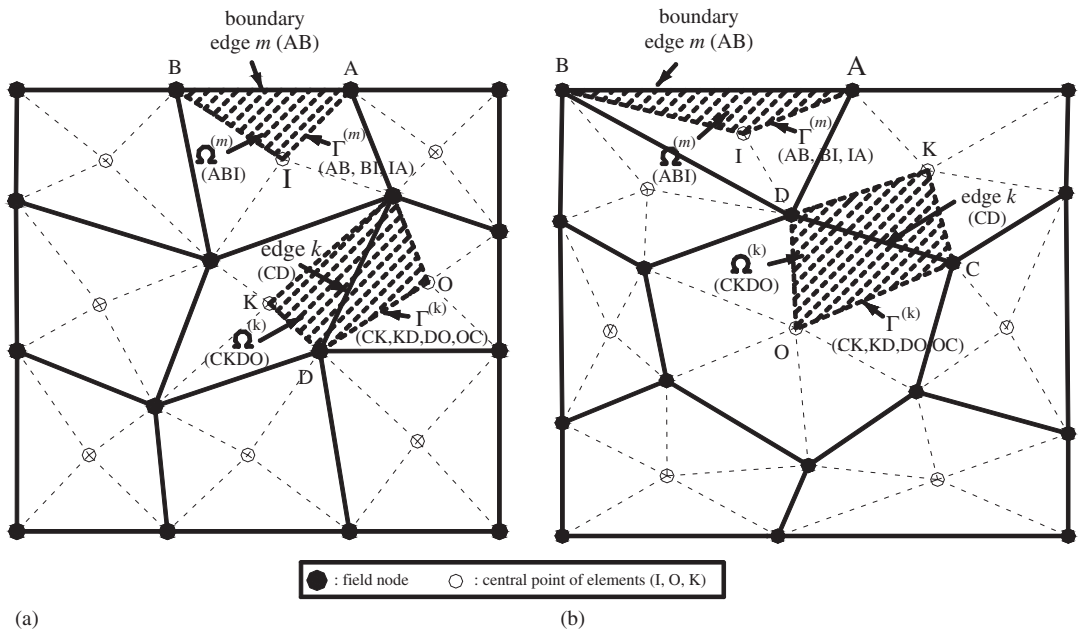


Figure 4. Domain discretization and the smoothing domains (shaded areas) associated with edges in the ES-FEM: (a) quadrilateral elements and (b) $n$-sided polygonal elements.

implementation of the FS-FEM is straightforward and no penalty parameter or additional degrees of freedom is used. The computational efficiency of the FS-FEM is found better than that of T4 element.

The paper is outlined as follows. In Section 2, the idea of the FS-FEM is introduced. In Section 3, the properties of the FS-FEM are presented and the geometrically non-linear problem of large deformation using the FS-FEM is described briefly in Section 4. Section 5 presents a domain-based selective scheme for nearly incompressible materials and numerical implementations of the FS-FEM are described in Section 6. Some numerical examples are presented and examined in Section 7 and some concluding remarks are made in Section 8.

## 2. THE IDEA OF THE FS-FEM

### *2.1. Briefing on the FEM* [*25–27*]

The discrete equations of the FEM are generated from the Galerkin weak form

$$\int_{\Omega} (\nabla_s \delta \mathbf{u})^{\mathrm{T}} \mathbf{D} (\nabla_s \mathbf{u}) \, \mathrm{d}\Omega - \int_{\Omega} \delta \mathbf{u}^{\mathrm{T}} \mathbf{b} \, \mathrm{d}\Omega - \int_{\Gamma_t} \delta \mathbf{u}^{\mathrm{T}} \bar{\mathbf{t}} \, \mathrm{d}\Gamma = 0 \tag{1}$$



DOI: 10.1002/nme

where $\mathbf{b}$ is the vector of external body forces, $\mathbf{D}$ is a symmetric positive-definite (SPD) matrix of material constants, $\bar{\mathbf{t}}$ is the prescribed traction vector on the natural boundary $\Gamma_t$, $\mathbf{u}$ is trial functions, $\delta\mathbf{u}$ is test functions and $\nabla_s\mathbf{u}$ is the symmetric gradient of the displacement field.

The FEM uses the following trial and test functions

$$\mathbf{u}^h(\mathbf{x}) = \sum_{I=1}^{\mathrm{NP}} \mathbf{N}_I(\mathbf{x})\,\mathbf{d}_I; \quad \delta\mathbf{u}^h(\mathbf{x}) = \sum_{I=1}^{\mathrm{NP}} \mathbf{N}_I(\mathbf{x})\delta\mathbf{d}_I \tag{2}$$

where NP is the number of the nodal variables of the element, $\mathbf{d}_I$ is the nodal displacement vector and $\mathbf{N}_I(\mathbf{x})$ is the shape function matrix.

By substituting the approximations, $\mathbf{u}^h$ and $\delta\mathbf{u}^h$, into the weak form and invoking the arbitrariness of virtual nodal displacements, Equation (1) yields the standard discretized algebraic equation system

$$\mathbf{K}^{\mathrm{FEM}}\mathbf{d} = \mathbf{f} \tag{3}$$

where $\mathbf{K}^{\mathrm{FEM}}$ is the stiffness matrix; $\mathbf{f}$ is the element force vector that are assembled with entries of

$$\mathbf{K}_{IJ}^{\mathrm{FEM}} = \int_\Omega \mathbf{B}_I^{\mathrm{T}}\mathbf{D}\mathbf{B}_J\,\mathrm{d}\Omega \tag{4}$$

$$\mathbf{f}_I = \int_\Omega \mathbf{N}_I^{\mathrm{T}}(\mathbf{x})\mathbf{b}\,\mathrm{d}\Omega + \int_{\Gamma_t} \mathbf{N}_I^{\mathrm{T}}(\mathbf{x})\bar{\mathbf{t}}\,\mathrm{d}\Gamma \tag{5}$$

with the *compatible strain gradient matrix* defined as

$$\mathbf{B}_I(\mathbf{x}) = \nabla_s\mathbf{N}_I(\mathbf{x}) \tag{6}$$

In the FEM, the integrations in Equations (4) and (5) are performed based on elements.

### 2.2. A face-based smoothed finite element method (FS-FEM)

This section formulates the FS-FEM for 3D problems using tetrahedral elements. In the FS-FEM, the domain discretization is the same as that of the standard FEM using $N_n$ nodes and $N_e$ tetrahedral elements, but the integration using strain-smoothing technique [6] is performed over smoothing domains constructed based on the faces of the elements. In such a face-based integration process, the problem domain $\Omega$ is divided into smoothing domains associated with faces of tetrahedral elements such that $\Omega = \sum_{k=1}^{N_f}\Omega^{(k)}$ and $\Omega^{(i)}\cap\Omega^{(j)} \neq \emptyset$, $i \neq j$, in which $N_f$ is the total number of faces located in the whole problem domain. For tetrahedral elements, the smoothing domain $\Omega^{(k)}$ associated with the face $k$ is created by connecting three nodes of the face to the two centers of the two adjacent elements as shown in Figure 5.

Applying the face-based smoothing operation, the *compatible* strains $\boldsymbol{\varepsilon} = \nabla_s\mathbf{u}$ used in Equation (1) is used to create a *smoothed* strain on the smoothing domain $\Omega^{(k)}$ associated with face $k$

$$\tilde{\boldsymbol{\varepsilon}}_k = \int_{\Omega^{(k)}} \boldsymbol{\varepsilon}(\mathbf{x})\Phi_k(\mathbf{x})\,\mathrm{d}\Omega = \int_{\Omega^{(k)}} \nabla_s\mathbf{u}(\mathbf{x})\Phi_k(\mathbf{x})\,\mathrm{d}\Omega \tag{7}$$

where $\Phi_k(\mathbf{x})$ is a given smoothing function that satisfies at least unity property

$$\int_{\Omega^{(k)}} \Phi_k(\mathbf{x})\,\mathrm{d}\Omega = 1 \tag{8}$$



DOI: 10.1002/nme

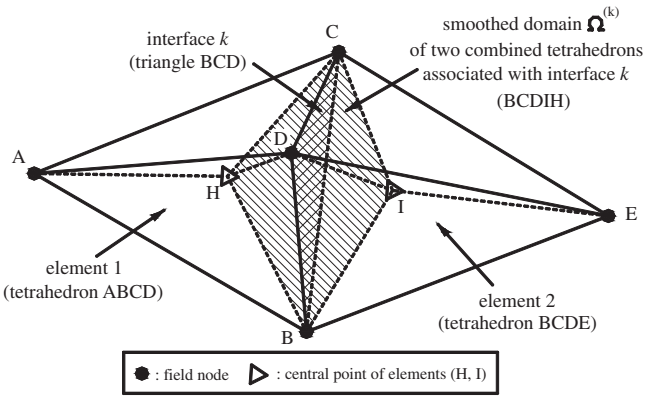


Figure 5. Two adjacent tetrahedral elements and the smoothing domain $\Omega^{(k)}$ (shaded domain) formed based on their interface $k$ in the FS-FEM.

Using the following constant smoothing function:

$$\Phi_k(\mathbf{x}) = \begin{cases} 1/V^{(k)}, & \mathbf{x} \in \Omega^{(k)} \\ 0, & \mathbf{x} \notin \Omega^{(k)} \end{cases} \tag{9}$$

where $V^{(k)}$ is the volume of the smoothing domain $\Omega^{(k)}$ and is calculated by

$$V^{(k)} = \int_{\Omega^{(k)}} \mathrm{d}\Omega = \frac{1}{4} \sum_{j=1}^{N_{\mathrm{e}}^{(k)}} V_{\mathrm{e}}^{(j)} \tag{10}$$

where $N_{\mathrm{e}}^{(k)}$ is the number of elements around the face $k$ ($N_{\mathrm{e}}^{(k)} = 1$ for the boundary faces and $N_{\mathrm{e}}^{(k)} = 2$ for inner faces) and $V_{\mathrm{e}}^{(j)}$ is the volume of the $j$th element around the face $k$.

In the FS-FEM, the trial function $\mathbf{u}^h(\mathbf{x})$ is the same as in Equation (2) of the FEM and therefore the force vector $\mathbf{f}$ in the FS-FEM is calculated in the same way as in the FEM.

Substituting Equation (2) into Equation (7), the smoothed strain on the domain $\Omega^{(k)}$ associated with face $k$ can be written in the following matrix form of nodal displacements:

$$\tilde{\boldsymbol{\varepsilon}}_k = \sum_{I \in N_{\mathrm{n}}^{(k)}} \tilde{\mathbf{B}}_I(\mathbf{x}_k)\, \mathbf{d}_I \tag{11}$$

where $N_{\mathrm{n}}^{(k)}$ is the total number of nodes of elements containing the common face $k$ ($N_{\mathrm{n}}^{(k)} = 4$ for boundary faces and $N_{\mathrm{n}}^{(k)} = 5$ for inner faces) and $\tilde{\mathbf{B}}_I(\mathbf{x}_k)$, which is termed as the *smoothed strain matrix* on the domain $\Omega^{(k)}$, is calculated numerically by an assembly process similarly as in the FEM

$$\tilde{\mathbf{B}}_I(\mathbf{x}_k) = \frac{1}{V^{(k)}} \sum_{j=1}^{N_{\mathrm{e}}^{(k)}} \frac{1}{4} V_{\mathrm{e}}^{(j)} \mathbf{B}_j \tag{12}$$

where $\mathbf{B}_j$ is the standard compatible strain gradient matrix by Equation (6) of the $j$th element around the face $k$.



DOI: 10.1002/nme

Owing to the use of the tetrahedral elements with the linear shape functions, the entries of matrix $\mathbf{B}_j$ are constants, and so are the entries of matrix $\tilde{\mathbf{B}}_I(\mathbf{x}_k)$. The entries in sub-matrices of the stiffness matrix $\tilde{\mathbf{K}}$ of the system are then assembled by a similar process as in the FEM

$$\tilde{\mathbf{K}}_{IJ} = \sum_{k=1}^{N_f} \tilde{\mathbf{K}}_{IJ}^{(k)} \tag{13}$$

where $\tilde{\mathbf{K}}_{IJ}^{(k)}$ is the stiffness matrix associated with face $k$ and is calculated by

$$\tilde{\mathbf{K}}_{IJ}^{(k)} = \int_{\Omega^{(k)}} \tilde{\mathbf{B}}_I^{\mathrm{T}} \mathbf{D} \tilde{\mathbf{B}}_J \, \mathrm{d}\Omega = \tilde{\mathbf{B}}_I^{\mathrm{T}} \mathbf{D} \tilde{\mathbf{B}}_J V^{(k)} \tag{14}$$

Note that with this formulation, only the volume and the usual compatible strain gradient matrices $\mathbf{B}_j$ by Equation (6) of T4 element are needed to calculate the system stiffness matrix for the FS-FEM.

Note that by applying the divergence theorem, the smoothed strain matrix $\tilde{\mathbf{B}}_I(\mathbf{x}_k)$ on the domain $\Omega^{(k)}$ can be calculated in a more general way by

$$\tilde{\mathbf{B}}_I(\mathbf{x}_k) = \frac{1}{V^{(k)}} \int_{\Gamma^{(k)}} \mathbf{n}^{(k)}(\mathbf{x}) \mathbf{N}_I(\mathbf{x}) \, \mathrm{d}\Gamma = \begin{bmatrix} \tilde{b}_{Ix}(\mathbf{x}_k) & 0 & 0 \\ 0 & \tilde{b}_{Iy}(\mathbf{x}_k) & 0 \\ 0 & 0 & \tilde{b}_{Iz}(\mathbf{x}_k) \\ \tilde{b}_{Iy}(\mathbf{x}_k) & \tilde{b}_{Ix}(\mathbf{x}_k) & 0 \\ 0 & \tilde{b}_{Iz}(\mathbf{x}_k) & \tilde{b}_{Iy}(\mathbf{x}_k) \\ \tilde{b}_{Iz}(\mathbf{x}_k) & 0 & \tilde{b}_{Ix}(\mathbf{x}_k) \end{bmatrix} \tag{15}$$

with

$$\tilde{b}_{Ih}(\mathbf{x}_k) = \frac{1}{V^{(k)}} \int_{\Gamma^{(k)}} n_h^{(k)}(\mathbf{x}) N_I(\mathbf{x}) \, \mathrm{d}\Gamma \quad (h = x, y, z) \tag{16}$$

where $\Gamma^{(k)}$ is the boundary of the smoothing domain $\Omega^{(k)}$, and $\mathbf{n}^{(k)}(\mathbf{x})$ is the outward normal vector matrix on the boundary $\Gamma^{(k)}$ and has the form

$$\mathbf{n}^{(k)}(\mathbf{x}) = \begin{bmatrix} n_x^{(k)} & 0 & 0 \\ 0 & n_y^{(k)} & 0 \\ 0 & 0 & n_z^{(k)} \\ n_y^{(k)} & n_x^{(k)} & 0 \\ 0 & n_z^{(k)} & n_y^{(k)} \\ n_z^{(k)} & 0 & n_x^{(k)} \end{bmatrix} \tag{17}$$

When a linear compatible displacement field along the boundary $\Gamma^{(k)}$ is used, one Gaussian point at the central point of the boundary areas $\Gamma_i^{(k)}$ of the smoothing domain $\Omega^{(k)}$ is sufficient



DOI: 10.1002/nme

for the area integration, the Equation (16) can be further simplified to its algebraic form

$$\tilde{b}_{Ih}(\mathbf{x}_k) = \frac{1}{V^{(k)}} \sum_{i=1}^{M} n_{ih}^{(k)} N_I(\mathbf{x}_i^{\mathrm{GP}}) A_i^{(k)} \quad (h = x, y, z) \tag{18}$$

where $M$ is the total number of the boundary areas $\Gamma_i^{(k)}$ ($M=6$ for the inner smoothing faces and $M=4$ for boundary smoothing faces), $\mathbf{x}_i^{\mathrm{GP}}$ is the central point (Gaussian point) of the boundary area $\Gamma_i^{(k)}$, whose area and outward unit normal are denoted as $A_i^{(k)}$ and $n_{ih}^{(k)}$, respectively.

Equation (18) implies that only shape function values at some particular points on the surfaces of the boundary domains $\Gamma_i^{(k)}$ are needed and no explicit analytical form is required. This gives much more freedom in shape function construction.

Note that by using Equation (15) to calculate $\tilde{\mathbf{B}}_I(\mathbf{x}_k)$, it is straightforward to extend the FS-FEM for the higher-order elements. However, to ensure stability, the number of smoothing domains should be increased corresponding to the number of nodes of the elements. The calculation of the minimum number of smoothing domains is given in Reference [8].

## 3. PROPERTIES OF THE FS-FEM

*Property 1* (*displacement compatibility*)
The assumed displacement field is compatible (linearly continuous through out the domain) in the FS-FEM.

This property can be explicitly seen from the FS-FEM formulation procedure: linear element-based interpolation is used throughout the whole problem domain. This property ensures that the FS-FEM will be able to reproduce the linear field exactly. This will be confirmed in the patch test given in Section 6.

*Property 2*
The FS-FEM is variationally consistent.

*Proof*
In the FS-FEM, the *generalized* Galerkin weak form is used with the smoothed strain (7) instead of the compatible strain $\boldsymbol{\varepsilon} = \nabla_{\mathrm{s}}\mathbf{u}$, the variational consistency thus needs to be examined. To this end, we start with the modified Hellinger–Reissner variational principle with the assumed strain vector $\tilde{\boldsymbol{\varepsilon}}$ and displacements $\mathbf{u}$ as independent field variables [28]

$$U(\mathbf{u}, \tilde{\boldsymbol{\varepsilon}}) = -\int_\Omega \frac{1}{2} \tilde{\boldsymbol{\varepsilon}}^{\mathrm{T}} \mathbf{D} \tilde{\boldsymbol{\varepsilon}} \, \mathrm{d}\Omega + \int_\Omega (\mathbf{D}\tilde{\boldsymbol{\varepsilon}})^{\mathrm{T}} (\nabla_{\mathrm{s}}\mathbf{u}) \, \mathrm{d}\Omega - \int_\Omega \mathbf{u}^{\mathrm{T}} \mathbf{b} \, \mathrm{d}\Omega - \int_{\Gamma_t} \mathbf{u}^{\mathrm{T}} \bar{\mathbf{t}} \, \mathrm{d}\Gamma \tag{19}$$

Performing the variation using the chain rule, one obtains

$$\begin{aligned} \delta U(\mathbf{u}, \tilde{\boldsymbol{\varepsilon}}) = &-\int_\Omega \delta\tilde{\boldsymbol{\varepsilon}}^{\mathrm{T}} \mathbf{D} \tilde{\boldsymbol{\varepsilon}} \, \mathrm{d}\Omega + \int_\Omega \delta\tilde{\boldsymbol{\varepsilon}}^{\mathrm{T}} \mathbf{D} (\nabla_{\mathrm{s}}\mathbf{u}) \, \mathrm{d}\Omega + \int_\Omega \tilde{\boldsymbol{\varepsilon}}^{\mathrm{T}} \mathbf{D} (\nabla_{\mathrm{s}}\delta\mathbf{u}) \, \mathrm{d}\Omega \\ &- \int_\Omega \delta\mathbf{u}^{\mathrm{T}} \mathbf{b} \, \mathrm{d}\Omega - \int_{\Gamma_{\mathrm{t}}} \delta\mathbf{u}^{\mathrm{T}} \bar{\mathbf{t}} \, \mathrm{d}\Gamma = 0 \end{aligned} \tag{20}$$



DOI: 10.1002/nme

Substituting the approximations (2), (11) into (20), one obtains

$$\sum_{I=1}^{N_n} \delta \mathbf{d}_I^T \left( -\int_\Omega \tilde{\mathbf{B}}_I^T \mathbf{D} \tilde{\mathbf{B}}_J \, d\Omega + \int_\Omega \tilde{\mathbf{B}}_I^T \mathbf{D} \mathbf{B}_J \, d\Omega + \int_\Omega \tilde{\mathbf{B}}_I^T \mathbf{D} \mathbf{B}_J \, d\Omega \right) \mathbf{d}_J$$

$$-\delta \mathbf{d}_I^T \left( \int_\Omega \mathbf{N}_I^T \mathbf{b} \, d\Omega + \int_{\Gamma_t} \mathbf{N}_I^T \bar{\mathbf{t}} \, d\Gamma \right) = 0, \quad J = \overline{1 : N_n}$$

and using the arbitrary property of variation, we obtain

$$\mathbf{K}^{\text{two-field}} \mathbf{d} = \mathbf{f} \tag{21}$$

where $\mathbf{K}^{\text{two-field}}$ is the *smoothed* stiffness matrix given by Equation (22), and $\mathbf{f}$ is the element force vector given by Equation (23)

$$\mathbf{K}_{IJ}^{\text{two-field}} = -\int_\Omega \tilde{\mathbf{B}}_I^T \mathbf{D} \tilde{\mathbf{B}}_J \, d\Omega + 2 \int_\Omega \tilde{\mathbf{B}}_I^T \mathbf{D} \mathbf{B}_J(\mathbf{x}) \, d\Omega \tag{22}$$

$$= -\sum_{k=1}^{N_f} \int_{\Omega^{(k)}} \tilde{\mathbf{B}}_I^T \mathbf{D} \tilde{\mathbf{B}}_J \, d\Omega + 2 \sum_{k=1}^{N_f} \int_{\Omega^{(k)}} \tilde{\mathbf{B}}_I^T \mathbf{D} \mathbf{B}_J(\mathbf{x}) \, d\Omega \tag{23}$$

Using smoothed matrices $\tilde{\mathbf{B}}_I$ in Equation (12), the following orthogonal condition is satisfied [29]

$$\int_{\Omega^{(k)}} \tilde{\mathbf{B}}_I^T \mathbf{D} \mathbf{B}_J(\mathbf{x}) \, d\Omega = \tilde{\mathbf{B}}_I^T \mathbf{D} \int_{\Omega^{(k)}} \mathbf{B}_J(\mathbf{x}) \, d\Omega = \tilde{\mathbf{B}}_I^T \mathbf{D} V^{(k)} \int_{\Omega^{(k)}} \frac{\mathbf{B}_J(\mathbf{x})}{V^{(k)}} \, d\Omega = \tilde{\mathbf{B}}_I^T \mathbf{D} \tilde{\mathbf{B}}_J V^{(k)}$$

$$= \int_{\Omega^{(k)}} \tilde{\mathbf{B}}_I^T \mathbf{D} \tilde{\mathbf{B}}_J \, d\Omega \tag{24}$$

and from Equation (22) we then have

$$\mathbf{K}_{IJ}^{\text{two-field}} = \tilde{\mathbf{K}}_{IJ}^{\text{FS-FEM}} = \int_\Omega \tilde{\mathbf{B}}_I^T \mathbf{D} \tilde{\mathbf{B}}_J \, d\Omega = \sum_{k=1}^{N_f} \int_{\Omega^{(k)}} \tilde{\mathbf{B}}_I^T \mathbf{D} \tilde{\mathbf{B}}_J \, d\Omega \tag{25}$$

The FS-FEM uses directly Equation (25) to calculate the stiffness matrix; therefore, the FS-FEM is 'variationally consistent'. □

Note that although the two-field Hellinger–Reissner principle is used, the FS-FEM has only the displacements as unknowns. Therefore, it is very much different from the so-called mixed FEM formulation, where stresses (or strains) are usually also unknowns.

*Property 3*
The stiffness matrix of the FS-FEM has the same unknowns of only the displacement, the same bandwidth and sparsity as that of the standard FEM, and hence the same computational complexity.

## 4. GEOMETRICALLY NON-LINEAR PROBLEMS OF LARGE DEFORMATION

For the geometrically non-linear problems of large deformation and isotropic linear elastic solids, the values of the strain gradient matrices and stresses at the faces are the average values of those of



DOI: 10.1002/nme

the adjacent elements around the face, and all the techniques used in the FEM can be employed. The finite element model of the FS-FEM for geometrically non-linear problems of large deformation based on the total Lagrange formulation [25, 30] is expressed as follows:

$$(\tilde{\mathbf{K}}_L^{\text{FS-FEM}} + \tilde{\mathbf{K}}_{NL}^{\text{FS-FEM}})\,\mathbf{d} = \mathbf{f} - \mathbf{f}_1 \tag{26}$$

where

$$\tilde{\mathbf{K}}_L^{\text{FS-FEM}} = \sum_{k=1}^{N_f} \tilde{\mathbf{B}}_L^{\mathrm{T}} \mathbf{D} \tilde{\mathbf{B}}_L V^{(k)} \tag{27}$$

$$\tilde{\mathbf{K}}_{NL}^{\text{FS-FEM}} = \sum_{k=1}^{N_f} \tilde{\mathbf{B}}_{NL}^{\mathrm{T}} \tilde{\mathbf{S}} \tilde{\mathbf{B}}_{NL} V^{(k)} \tag{28}$$

$$\mathbf{f}_1 = \sum_{k=1}^{N_f} \tilde{\mathbf{B}}_L^{\mathrm{T}} \{\tilde{\mathbf{S}}\} V^{(k)} \tag{29}$$

With

$$\mathbf{B}_L = \begin{bmatrix} F_{11}N_{1,1} & F_{21}N_{1,1} & F_{31}N_{1,1} \\ F_{12}N_{1,2} & F_{22}N_{1,2} & F_{13}N_{1,2} \\ F_{13}N_{1,3} & F_{23}N_{1,3} & F_{33}N_{1,3} \\ F_{11}N_{1,2}+F_{12}N_{1,1} & F_{21}N_{1,2}+F_{22}N_{1,1} & F_{31}N_{1,2}+F_{32}N_{1,1} \\ F_{12}N_{1,3}+F_{13}N_{1,2} & F_{22}N_{1,3}+F_{23}N_{1,2} & F_{32}N_{1,3}+F_{33}N_{1,2} \\ F_{11}N_{1,3}+F_{13}N_{1,1} & F_{21}N_{1,3}+F_{23}N_{1,1} & F_{31}N_{1,3}+F_{33}N_{1,1} \end{bmatrix}$$

$$\begin{bmatrix} F_{11}N_{2,1} & \cdots & F_{31}N_{4,1} \\ F_{12}N_{2,2} & \cdots & F_{13}N_{4,2} \\ F_{13}N_{2,3} & \cdots & F_{33}N_{4,3} \\ F_{11}N_{2,2}+F_{12}N_{2,1} & \cdots & F_{31}N_{4,2}+F_{32}N_{4,1} \\ F_{12}N_{2,3}+F_{13}N_{2,2} & \cdots & F_{32}N_{4,3}+F_{33}N_{4,2} \\ F_{11}N_{2,3}+F_{13}N_{2,1} & \cdots & F_{31}N_{4,3}+F_{33}N_{4,1} \end{bmatrix} \tag{30}$$

$$\tilde{\mathbf{B}}_L = \frac{1}{V^{(k)}} \sum_{i=1}^{N_e^{(k)}} \frac{1}{4} V_e^{(i)} \mathbf{B}_L^{(i)} \tag{31}$$



DOI: 10.1002/nme

$$\mathbf{B}_{NL}=\begin{bmatrix} N_{1,1} & 0 & 0 & N_{2,1} & \cdots & 0 \\ N_{1,2} & 0 & 0 & N_{2,2} & \cdots & 0 \\ N_{1,3} & 0 & 0 & N_{2,3} & \cdots & 0 \\ 0 & N_{1,1} & 0 & 0 & \cdots & 0 \\ 0 & N_{1,2} & 0 & 0 & \cdots & 0 \\ 0 & N_{1,3} & 0 & 0 & \cdots & 0 \\ 0 & 0 & N_{1,1} & 0 & \cdots & N_{4,1} \\ 0 & 0 & N_{1,2} & 0 & \cdots & N_{4,2} \\ 0 & 0 & N_{1,3} & 0 & \cdots & N_{4,3} \end{bmatrix} \quad \text{and} \quad \tilde{\mathbf{B}}_{NL}=\frac{1}{V^{(k)}}\sum_{i=1}^{N_{\mathrm{e}}^{(k)}}\frac{1}{4}V_{\mathrm{e}}^{(i)}\mathbf{B}_{NL}^{(i)} \tag{32}$$

$$\mathbf{S}=\begin{bmatrix} S_{11} & S_{12} & S_{13} & 0 & 0 & 0 & 0 & 0 & 0 \\ S_{12} & S_{22} & S_{23} & 0 & 0 & 0 & 0 & 0 & 0 \\ S_{13} & S_{23} & S_{33} & 0 & 0 & 0 & 0 & 0 & 0 \\ 0 & 0 & 0 & S_{11} & S_{12} & S_{13} & 0 & 0 & 0 \\ 0 & 0 & 0 & S_{12} & S_{22} & S_{23} & 0 & 0 & 0 \\ 0 & 0 & 0 & S_{13} & S_{23} & S_{33} & 0 & 0 & 0 \\ 0 & 0 & 0 & 0 & 0 & 0 & S_{11} & S_{12} & S_{13} \\ 0 & 0 & 0 & 0 & 0 & 0 & S_{12} & S_{22} & S_{23} \\ 0 & 0 & 0 & 0 & 0 & 0 & S_{13} & S_{23} & S_{33} \end{bmatrix} \quad \text{and}$$

$$\tilde{\mathbf{S}}=\frac{1}{V^{(k)}}\sum_{i=1}^{N_{\mathrm{e}}^{(k)}}\frac{1}{4}V_{\mathrm{e}}^{(i)}\mathbf{S}^{(i)} \tag{33}$$

where the second Piola-Kirchhoff stress tensor $\{\mathbf{S}\}$ is derived from

$$\{\mathbf{S}\}=\begin{bmatrix} S_{11} \\ S_{22} \\ S_{33} \\ S_{12} \\ S_{23} \\ S_{31} \end{bmatrix}=\mathbf{D}\begin{bmatrix} E_{11} \\ E_{22} \\ E_{33} \\ 2E_{12} \\ 2E_{23} \\ 2E_{31} \end{bmatrix} \quad \text{and} \quad \{\tilde{\mathbf{S}}\}=\frac{1}{V^{(k)}}\sum_{i=1}^{N_{\mathrm{e}}^{(k)}}\frac{1}{4}V_{\mathrm{e}}^{(i)}\{\mathbf{S}\}^{(i)} \tag{34}$$

with the Green–Lagrange strain tensor $\mathbf{E}$ of the elements is calculated by

$$\mathbf{E}=\begin{bmatrix} E_{11} & E_{12} & E_{13} \\ E_{21} & E_{22} & E_{23} \\ E_{31} & E_{32} & E_{33} \end{bmatrix}=\frac{1}{2}(\mathbf{F}^{\mathrm{T}}\mathbf{F}-\mathbf{I}) \tag{35}$$



DOI: 10.1002/nme

where $\mathbf{I}$ is the third-order unit matrix and the deformation gradient tensor $\mathbf{F}$ of the elements is derived from

$$\mathbf{F}=\begin{bmatrix} F_{11} & F_{12} & F_{13} \\ F_{21} & F_{22} & F_{23} \\ F_{31} & F_{32} & F_{33} \end{bmatrix}=\left(\frac{\partial \mathbf{x}}{\partial \mathbf{X}}\right)^{\mathrm{T}}=(\nabla \mathbf{d}+\mathbf{I})^{\mathrm{T}} \tag{36}$$

Note that in Equations (30) and (32), $N_{I,j}=\partial N_I/\partial X_j$.

## 5. A DOMAIN-BASED SELECTIVE SCHEME: A COMBINED FS/NS-FEM MODEL

Volumetric locking appears when the Poisson's ratio approaches 0.5. The application of selective formulations in the conventional FEM [31] has been found effectively to overcome such a locking and hence the similar idea is employed in this paper. However, different from the FEM using selective integration [31], our selective scheme will use two different types of smoothing domains selectively for two different material 'parts' ($\mu$-part and $\lambda$-part). Since the node-based smoothing domains used in the NS-FEM were found effective in overcoming volumetric locking [16], and the $\lambda$-part is known as the culprit of the volume locking, we use node-based domains for the $\lambda$-part and face-based domains for the $\mu$-part. The details are given below:

The material property matrix $\mathbf{D}$ for isotropic materials is first decomposed into

$$\mathbf{D}=\mathbf{D}_1+\mathbf{D}_2 \tag{37}$$

where $\mathbf{D}_1$ relates to the shearing modulus $\mu=E/[2(1+\nu)]$ and hence is termed as $\mu$-part of $\mathbf{D}$, and $\mathbf{D}_2$ relates to the Lame's parameter $\lambda=2\nu\mu/(1-2\nu)$ and hence is termed as $\lambda$-part of $\mathbf{D}$. For 3D geometries, we have:

$$\mathbf{D}=\mu\begin{bmatrix} 2 & 0 & 0 & 0 & 0 & 0 \\ 0 & 2 & 0 & 0 & 0 & 0 \\ 0 & 0 & 2 & 0 & 0 & 0 \\ 0 & 0 & 0 & 1 & 0 & 0 \\ 0 & 0 & 0 & 0 & 1 & 0 \\ 0 & 0 & 0 & 0 & 0 & 1 \end{bmatrix}+\lambda\begin{bmatrix} 1 & 1 & 1 & 0 & 0 & 0 \\ 1 & 1 & 1 & 0 & 0 & 0 \\ 1 & 1 & 1 & 0 & 0 & 0 \\ 0 & 0 & 0 & 0 & 0 & 0 \\ 0 & 0 & 0 & 0 & 0 & 0 \\ 0 & 0 & 0 & 0 & 0 & 0 \end{bmatrix}=\mathbf{D}_1+\mathbf{D}_2 \tag{38}$$

In our domain-based selective scheme proposed, we use the NS-FEM to calculate the stiffness matrix related to $\lambda$-part and the FS-FEM to calculate the one related to the $\mu$-part. The stiffness matrix of the combined FS/NS-FEM model becomes

$$\tilde{\mathbf{K}}=\underbrace{\sum_{i=1}^{N_{\mathrm{f}}}(\tilde{\mathbf{B}}_1^i)^{\mathrm{T}}\mathbf{D}_1\tilde{\mathbf{B}}_1^i V_1^i}_{\tilde{\mathbf{K}}_1^{\text{FS-FEM}}}+\underbrace{\sum_{j=1}^{N_{\mathrm{n}}}(\tilde{\mathbf{B}}_2^j)^{\mathrm{T}}\mathbf{D}_2\tilde{\mathbf{B}}_2^j V_2^j}_{\tilde{\mathbf{K}}_2^{\text{NS-FEM}}} \tag{39}$$

where $\tilde{\mathbf{B}}_1^i$ and $V_1^i$ are the smoothed strain matrix and volume of the smoothing domain $\Omega_{\mathrm{f}}^{(i)}$ associated with face $i$, correspondingly; $\tilde{\mathbf{B}}_2^j$ and $V_2^j$ are the smoothed strain matrix and volume



DOI: 10.1002/nme

of the smoothing domain $\Omega_n^{(j)}$ associated with node $j$, correspondingly; $N_n$ is the total number of nodes located in the entire problem domain.

## 6. NUMERICAL IMPLEMENTATION

### 6.1. Stability of the FS-FEM

*Property 4*
The FS-FEM possesses only 'legal' zero energy modes that represent the rigid motions and hence the FS-FEM is spatially stable. There exist no spurious non-zero energy modes and thus the FS-FEM is also temporally stable.

In the standard FEM using T4 meshes and linear shape functions, the integration on the weak form is based on elements. For each element, only one Gauss point is needed to calculate. This implies that the number of Gauss points to calculate equals to the number of elements of the problem. Such an FEM model is known to be stable in dynamics analysis and has no spurious non-zero energy modes.

In the FS-FEM using T4 meshes, the smoothing domains used are associated with faces and the strain (or stress) on each domain is constant. Therefore, each domain is considered equivalent to using one Gauss point to calculate the weak form. Because the number of faces is always larger than the number of elements in any mesh, the number of Gauss points to calculate the weak form in the FS-FEM is always larger than that in the FEM. Therefore, the FS-FEM is also very stable and has no spurious non-zero energy modes, and is well suited for the dynamic analysis. This property of the FS-FEM is quite similar to that of the ES-FEM for free and forced vibration analyses of solids in 2D problems [23].

Note that, in the NS-FEM [16], the smoothing domains used are associated with the node. The NS-FEM is proven spatially stable, works well for static problems and can produce upper bound solutions. However for vibration analysis, the NS-FEM is unstable due to the presence of spurious non-zero energy modes. This is because the number of nodes is usually much smaller than the number of elements. This is the same as the under-integration of the weak form inherent in the nodal integration approach of meshfree methods. The temporal instability, therefore, is one of the main concerns of the NS-FEM and meshfree methods [3, 32–35].

### 6.2. Procedure of the FS-FEM

The numerical procedure for the FS-FEM is briefly given as follows:

1. Divide the domain into a set of elements and obtain information on nodes coordinates and element connectivity,
2. Determine the adjacent elements and the smoothing domain $\Omega^{(k)}$ associated with each face $k$,
3. Loop over all the elements
   (a) Compute and save the gradient matrix $\mathbf{B}$ of the element by Equation (6),
   (b) Evaluate the force vector of the element by Equation (5), and assemble force vector into the global force vector,



DOI: 10.1002/nme

4. Loop over all the faces
   (a) Compute the matrix $\tilde{\mathbf{B}}_I(\mathbf{x}_k)$ using Equation (12),
   (b) Evaluate the stiffness matrix using Equation (14) of the current smoothing domain $\Omega^{(k)}$,
   (c) Assemble the contribution of the current smoothing domain to form the system stiffness matrix using Equation (13),
5. Implement essential boundary conditions,
6. Solve the system equations to obtain the nodal displacements,
7. Evaluate strains and stresses at interested points.

### *6.3. Irons first-order patch test and a mesh sensitivity analysis*

A first-order patch test is a necessary requirement as a means of assessing the convergence of a numerical method based on Galerkin weak form. Linear displacements are imposed along the exterior boundaries of a cubic patch with at least one interior node. Satisfaction of the patch test requires that the displacements of all the interior nodes follow 'exactly' (to machine precision) the same function of the imposed displacement and constant strain/stress states are reproduced.

The related parameters are taken as $E=6.895\times10^6$ kPa, $v=0.25$ and linear displacement field is given by

$$\begin{aligned} u &= 0.001*(2x+y+z)/2 \\ v &= 0.001*(x+2y+z)/2 \\ w &= 0.001*(x+y+2z)/2 \end{aligned} \tag{40}$$

The following error norm in displacements is used to examine the computed results:

$$e_{\mathrm{d}}=\frac{\sum_{i=1}^{\mathrm{ndof}}|u_i-u_i^h|}{\sum_{i=1}^{\mathrm{ndof}}|u_i|}\times100\% \tag{41}$$

where $u_i$ is the exact solution and $u_i^h$ is the numerical solution. The energy error is defined by

$$e_{\mathrm{e}}=|E_{\mathrm{num}}-E_{\mathrm{exact}}| \tag{42}$$

where the total strain energy of numerical solution $E_{\mathrm{num}}$ and the total strain energy of exact solution $E_{\mathrm{exact}}$ are calculated by

$$E_{\mathrm{num}}=\frac{1}{2}\sum_{k=1}^{N_{\mathrm{f}}}(\boldsymbol{\varepsilon}_k^h)^{\mathrm{T}}\mathbf{D}\boldsymbol{\varepsilon}_k^h V^{(k)} \quad \text{or} \quad E_{\mathrm{num}}=\frac{1}{2}\mathbf{d}^{\mathrm{T}}\mathbf{K}\mathbf{d} \tag{43}$$

$$E_{\mathrm{exact}}=\tfrac{1}{2}\boldsymbol{\varepsilon}^{\mathrm{T}}\mathbf{D}\boldsymbol{\varepsilon}V_{\mathrm{cubic}} \tag{44}$$

where $\boldsymbol{\varepsilon}$ is the constant strain of exact solution; $\boldsymbol{\varepsilon}_k^h$ is the strain of numerical solution of the $k$th face; $V_{\mathrm{cubic}}$ is the volume of the cubic patch.

A spatial discretization of a cubic patch using 29 T4 elements and 15 nodes (including 8 nodes at the corners, 6 nodes at the center of 6 boundary faces and 1 interior node) is shown in Figure 6.



DOI: 10.1002/nme

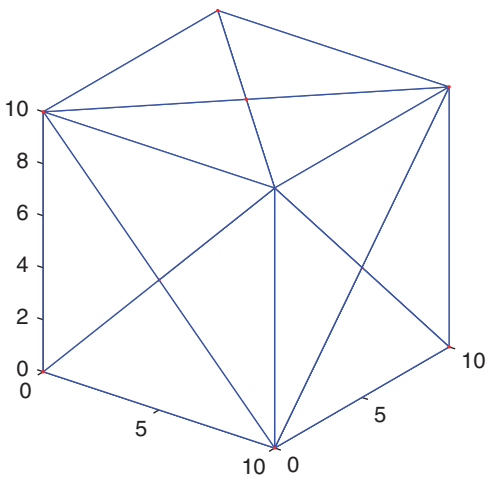


Figure 6. Domain discretization of a cubic patch using 4-node tetrahedral elements.

Table I. Displacement and energy error norms of the patch test.

| | $\alpha_{ir}=0.0$ | $\alpha_{ir}=0.1$ | $\alpha_{ir}=0.2$ | $\alpha_{ir}=0.3$ | $\alpha_{ir}=0.4$ | $\alpha_{ir}=0.49$ |
|---|---|---|---|---|---|---|
| Displacement norm $e_d$ (%) | 3.95e−16 | 1.16e−15 | 7.73e−16 | 1.00e−15 | 1.53e−15 | 2.21e−15 |
| Energy norm $e_e$ | 0.0 | 7.28e−12 | 1.82e−11 | 1.09e−11 | 7.28e−12 | 2.12e−11 |

In order to analyze the sensitivity for highly distorted meshes, two types of discretization are used, one with the interior node located at the center of the cubic patch and one with the interior node moved randomly inside the cubic patch from the center point in the following fashion:

$$\begin{aligned} x' &= x+\Delta x\cdot r_x\cdot\alpha_{ir} \\ y' &= y+\Delta y\cdot r_y\cdot\alpha_{ir} \\ z' &= z+\Delta z\cdot r_z\cdot\alpha_{ir} \end{aligned} \tag{45}$$

where $x$, $y$ and $z$ are the coordinate at the center point of the cubic patch; $\Delta x$, $\Delta y$ and $\Delta z$ are length of the cubic patch in the $x$-, $y$- and $z$-directions, respectively. $r_x$, $r_y$ and $r_z$ is computer-generated random numbers between $-1.0$ and 1.0 and $\alpha_{ir}$ is a prescribed irregularity factor whose value is chosen between 0.0 and 0.49. When $\alpha_{ir}=0.0$, the interior node locates at the center point of the cubic patch, and when $\alpha_{ir}>0.0$, the interior node moves randomly inside the cubic patch. The bigger the value of $\alpha_{ir}$, the more irregular the shape of elements generated.

It is found that the FS-FEM can pass the Irons first-order patch test within machine precision regardless of the value $\alpha_{ir}$ used as shown in Table I. There is no accuracy loss due to the choice of $\alpha_{ir}$ value. This shows that the FS-FEM can work well with the severe distorted meshes. The FS-FEM, therefore, is suitable to solve the geometrically non-linear problems of large deformation.



DOI: 10.1002/nme

## 7. NUMERICAL EXAMPLES

In this section, some examples will be presented to demonstrate the properties of the present method. In some cases, to emphasize the advantages of the FS-FEM, the results of the present method will be compared with those of the FEM using tetrahedral elements (FEM-T4), 8-node hexahedral elements (FEM-H8) and NS-FEM using tetrahedral elements (NS-FEM-T4) [16].

The error norm of displacement is given by Equation (41), and the error norm of energy is calculated by

$$e_{\mathrm{e}} = |E_{\mathrm{num}} - E_{\mathrm{exact}}|^{1/2} \tag{46}$$

where the total strain energy of numerical solution $E_{\mathrm{num}}$ and the total strain energy of exact solution $E_{\mathrm{exact}}$ are calculated by

$$E_{\mathrm{num}} = \tfrac{1}{2}\mathbf{d}^{\mathrm{T}}\mathbf{K}_{\mathrm{num}}\mathbf{d} \tag{47}$$

$$E_{\mathrm{exact}} = \frac{1}{2}\lim_{N_{\mathrm{e}}\to\infty}\sum_{i=1}^{N_{\mathrm{e}}}\int_{\Omega_i}\boldsymbol{\varepsilon}_i^{\mathrm{T}}\mathbf{D}\,\boldsymbol{\varepsilon}_i\,\mathrm{d}\Omega \tag{48}$$

where $\boldsymbol{\varepsilon}_i$ is the strain of exact solution of the $i$th element. In actual computation using Equation (46), we will use a very fine mesh ($N_{\mathrm{e}}\to\infty$) to calculate the exact strain energy $E_{\mathrm{exact}}$.

### *7.1. 3D Lame problem*

A 3D Lame problem consists of a hollow sphere with inner radius $a=1$ m, outer radius $b=2$ m and subjected to internal pressure $P=1\,\mathrm{N/m^2}$, as shown in Figure 7. For this benchmark problem, the analytical solution is available in polar coordinate system [36].

$$u_r = \frac{Pa^3 r}{E(b^3-a^3)}\left[(1-2v)+(1+v)\frac{b^3}{2r^3}\right] \tag{49}$$

$$\sigma_r = \frac{Pa^3(b^3-r^3)}{r^3(a^3-b^3)}; \quad \sigma_\theta = \frac{Pa^3(b^3+2r^3)}{2r^3(b^3-a^3)} \tag{50}$$

where $r$ is the radial distance from the centroid of the sphere to the point of interest in the sphere.

As the problem is spherically symmetrical, only one-eighth of the sphere model is shown in Figure 8 and symmetry conditions are imposed on the three symmetric planes. The material parameters of the problem are $E=1.0\,\mathrm{kPa}$ and $v=0.3$.

Figure 9 shows the convergence rate of the energy error norm of different methods. It is seen that the results of the FS-FEM and FEM-H8 are almost the same and much more accurate than those of the NS-FEM-T4 and FEM-T4. Figure 10 shows that the distribution of the radial displacement using the FS-FEM is in a good agreement with the analytical solution. Figure 11 shows the convergence rate of the displacement error norm of the different methods. It is shown that the result of the FS-FEM is less accurate than that of the FEM-H8 but more accurate than those of the NS-FEM-T4 and FEM-T4. All the above results show that the FS-FEM is significantly more accurate than the FEM-T4 using tetrahedral elements in the 3D linear problems.



DOI: 10.1002/nme

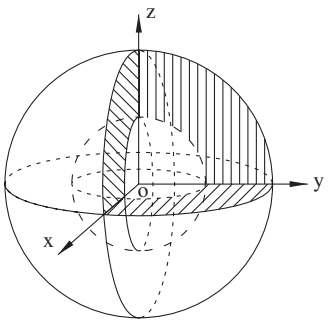


Figure 7. Hollow sphere model.

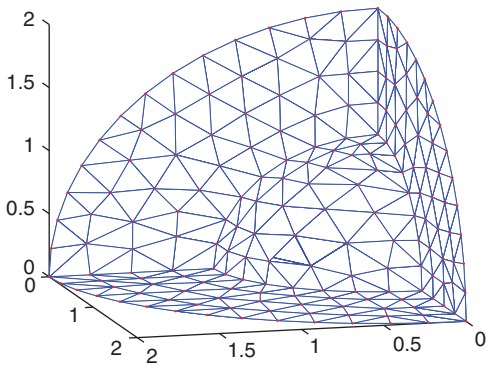


Figure 8. Discretization of one-eighth of hollow sphere model using 4-node tetrahedral elements.

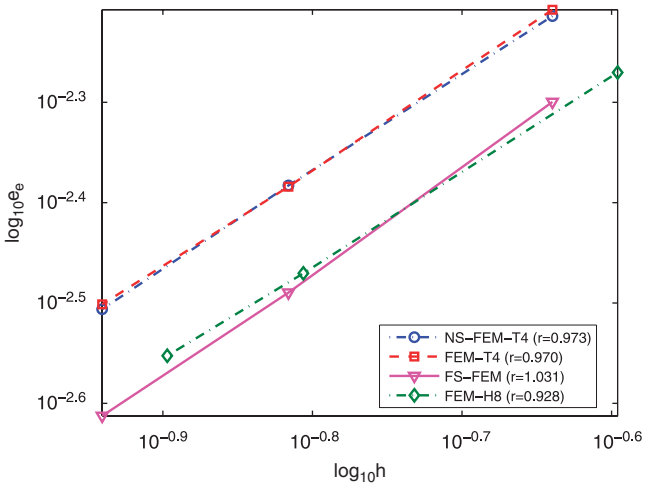


Figure 9. Convergence rate of energy error norm of the hollow sphere subjected to inner pressure.



DOI: 10.1002/nme

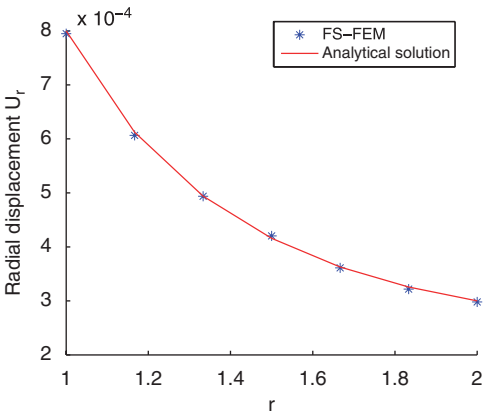


Figure 10. Distribution of the radial displacement of the hollow sphere subjected to inner pressure.

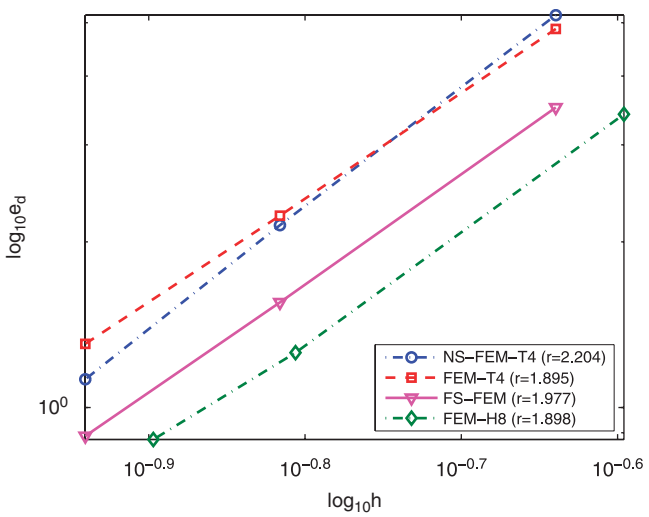


Figure 11. Convergence rate of displacement error norm of the hollow sphere subjected to inner pressure.

Figure 12 shows the displacement error norm for nearly incompressible material when Poisson's ratio is changed from 0.4 to 0.4999999. The results show that the domain-based selective FS/NS-FEM-T4 can overcome the volumetric locking for nearly incompressible materials and gives better results than those of the NS-FEM-T4.

Figure 13 compares the computational time between FEM-T4 and FS-FEM. It is seen that with the same set of nodes, the FS-FEM takes a longer time to solve than the FEM-T4. However, the FS-FEM is found to be more efficient than the FEM-T4 in terms of CPU time for the same accuracy in both energy and displacement error norms as shown in Figures 14 and 15.



DOI: 10.1002/nme

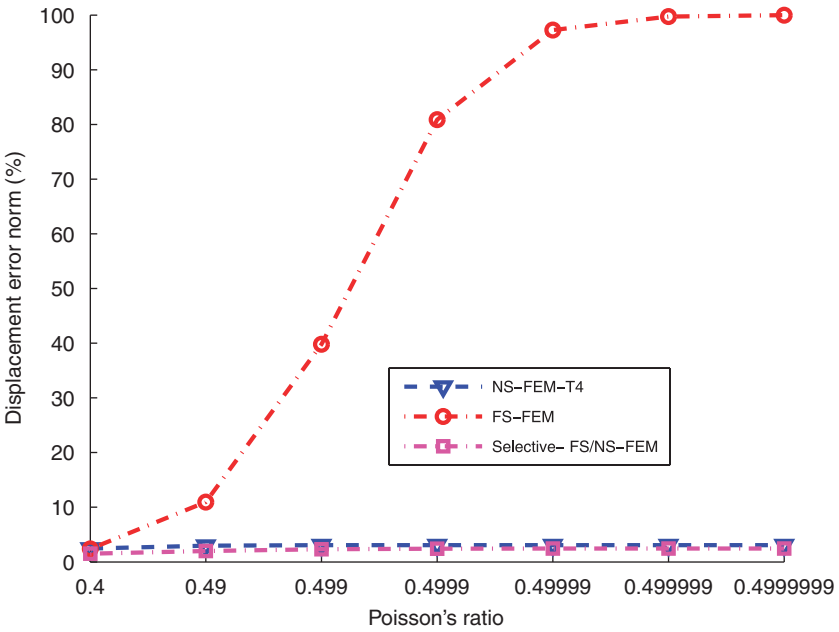


Figure 12. Displacement error norm versus different Poisson ratios of the hollow sphere subjected to inner pressure.

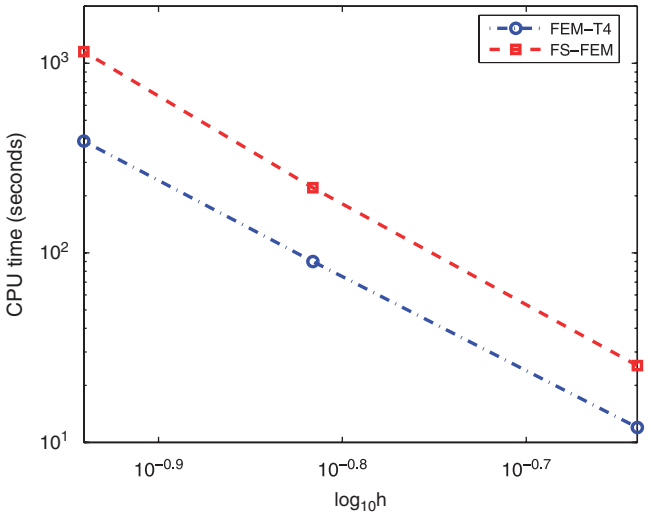


Figure 13. Comparison of the computational time between FEM-T4 and FS-FEM of the hollow sphere subjected to inner pressure.



DOI: 10.1002/nme

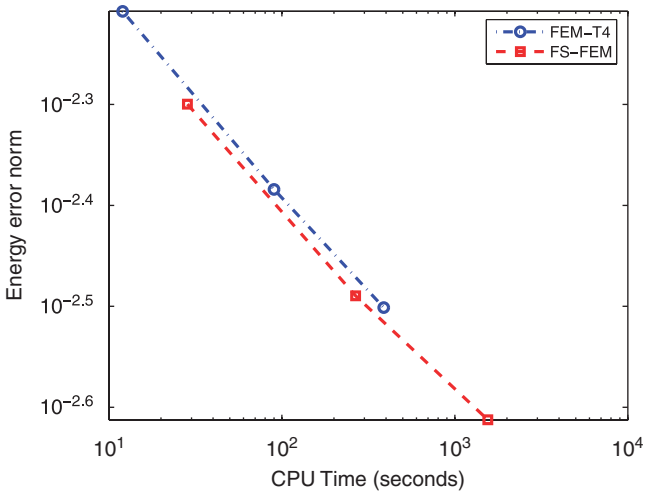


Figure 14. Comparison of the efficiency in terms of energy error norm between FEM-T4 and FS-FEM of the hollow sphere subjected to inner pressure.

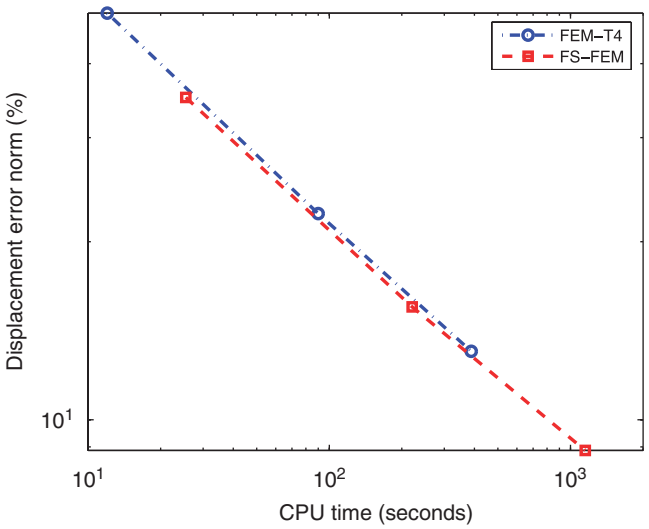


Figure 15. Comparison of the efficiency in terms of displacement error norm between FEM-T4 and FS-FEM of the hollow sphere subjected to inner pressure.

### *7.2. A 3D cubic cantilever*

Consider a 3D cantilever of cubic shape, subjected to a uniform pressure on its upper face as shown in Figure 16. A discretization of the 3D cubic cantilever using tetrahedral elements is shown in Figure 17. The exact solution of the problem is unknown. Using standard FEM and a very fine mesh with 30 204 nodes and 20 675 10-node tetrahedron elements, a reference solution of



DOI: 10.1002/nme

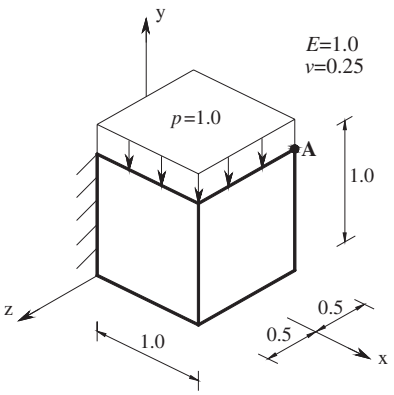


Figure 16. A 3D cubic cantilever subjected to a uniform pressure on the top surface.

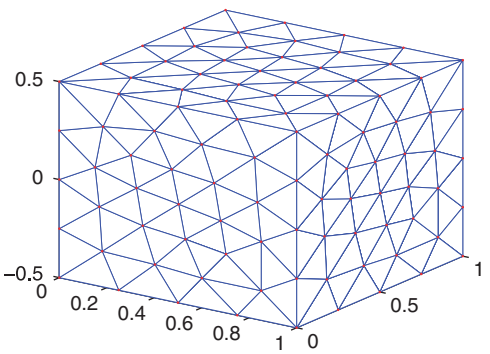


Figure 17. A discretization of the 3D cubic cantilever subjected to a uniform pressure on the top surface using 4-node tetrahedral elements.

the strain energy is found to be $E=0.9486$. Also from this reference, the deflection at point A $(1.0, 1.0, -0.5)$ is 3.3912.

Figures 18 and 19 show the convergence rate of energy error norm and relative deflection error at point A of the different methods, respectively. It is shown that the results of the FS-FEM are a little less accurate than that of the FEM-H8, but much more accurate than those of the NS-FEM-T4 and FEM-T4. These results again show that the FS-FEM is significantly more accurate than the FEM-T4 using tetrahedral elements in 3D linear problems.

### *7.3. A 3D cantilever beam subjected to a regular distributed load: a geometrically non-linear analysis of large deformation*

This example examines the use of the FS-FEM for the geometrically non-linear analysis of large deformation for 3D solids. A 3D cantilever beam subjected to a regular distributed load is considered. The size of the beam is $(10\,\text{cm} \times 2\,\text{cm} \times 2\,\text{cm})$ and discretized using a mesh including 1322



DOI: 10.1002/nme

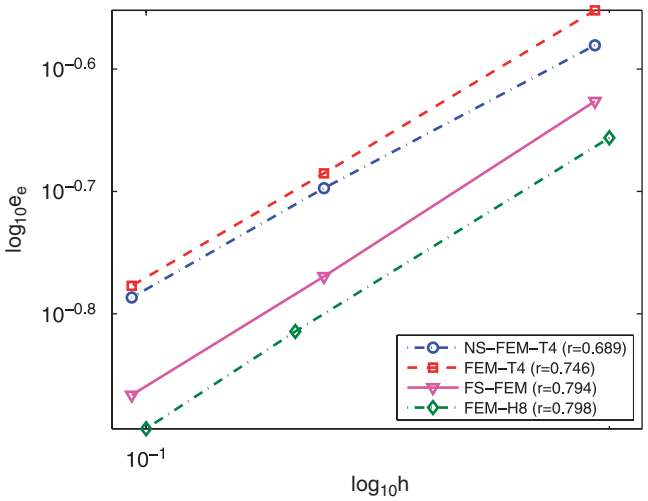


Figure 18. Convergence rate of the energy error norm of the cubic cantilever subjected to a uniform pressure on the top surface.

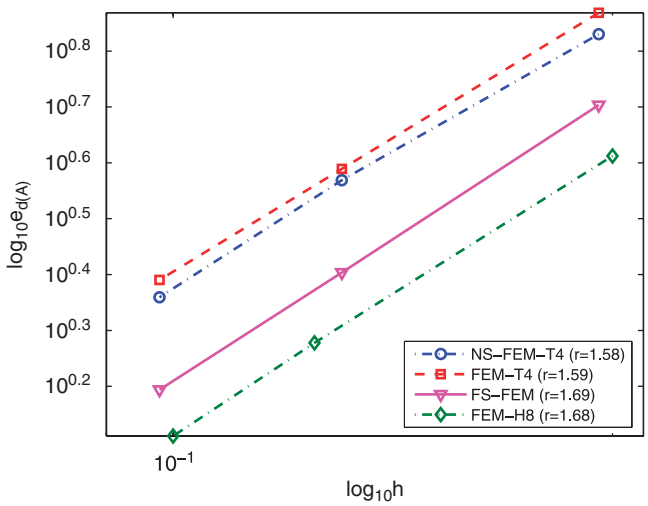


Figure 19. Convergence rate of the deflection at point A(1.0, 1.0, −0.5) of the cubic cantilever subjected to a uniform pressure on the top surface.

nodes and 5802 tetrahedral elements as shown in Figure 21. The related parameters are taken as $E = 3.0 \times 10^7$ kPa, $v = 0.3$.

First, a mesh sensitivity analysis using the FS-FEM and the FEM-T4 is performed in the similar way as in the Iron first-order patch test. The interior nodes are moved randomly inside the cantilever beam from the original regular positions based on Equation (45), where $x$, $y$ and $z$ are the original coordinates of interior points; $\Delta x$, $\Delta y$ and $\Delta z$ are original average length of the element in the



DOI: 10.1002/nme

Table II. Tip deflection (cm) versus the irregularity factor $\alpha_{ir}$ of the 3D cantilever beam subjected to a regular distributed load.

| | $\alpha_{ir}=0.0$ | $\alpha_{ir}=0.1$ | $\alpha_{ir}=0.2$ | $\alpha_{ir}=0.3$ | $\alpha_{ir}=0.4$ |
|---|---|---|---|---|---|
| FS-FEM (1322 nodes) | 2.4429 | 2.4373 (0.23%)* | 2.4218 (0.86%) | 2.3888 (2.21%) | 2.3418 (4.14%) |
| FEM-T4 (1322 nodes) | 2.3639 | 2.3559 (0.34%) | 2.3349 (1.23%) | 2.2933 (2.99%) | 2.2141 (6.34%) |

*The number in the bracket shows the relative error (%) between the numerical results at $\alpha_{ir}>0$ and that at $\alpha_{ir}=0.0$.

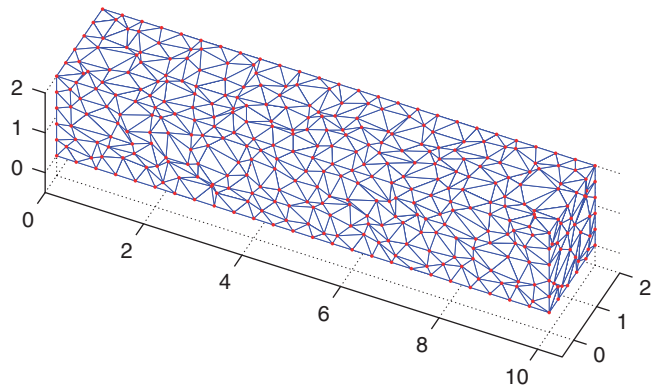


Figure 20. A domain discretization of the 3D cantilever beam subjected to a regular distributed load using severe distorted tetrahedral elements.

$x$-, $y$- and $z$-directions, respectively. In addition, the interior nodes of boundary faces are also moved randomly inside their original faces. Only nodes located on the boundary sides of the cantilever beam are kept unchanged. Table II shows the relation between the tip deflection versus the prescribed irregularity factor $\alpha_{ir}$ chosen between 0.0 and 0.4, and Figure 20 demonstrates a severe distorted mesh discretization at $\alpha_{ir}=0.4$. Using the tip deflection $d=2.5061$ of the FEM-H8 (1323 nodes) as a reference solution, the results in Table II show that the FS-FEM works more accurately and is less sensitive with the distortion of the mesh than those of the FEM-T4. The FS-FEM is therefore much more suitable than the FEM-T4 for geometrically non-linear analysis of large deformation.

The geometrically non-linear analysis based on the total Lagrange formulation is carried out using 10 increment steps ($n=10$) with $\Delta f=4\text{kN/cm}^2$ in each step. Figure 21 displays the initial and final configurations after 10 steps of increment of the deformation using the FS-FEM. Table III and Figure 22 show the relation between the tip deflection versus the load step of different methods. The simulation converges at a very rapid speed and in each load increment, only less than five times of iteration are performed. It can be seen that the non-linear effects make the cantilever beam behave stiffer compared with the linear solutions. In the geometrically non-linear analysis, the results of FS-FEM are softer than those of FEM-T4, but stiffer than those of the FEM-H8 using 1323 nodes. All these results suggest that the FS-FEM also performs more accurately than the FEM-T4 in 3D geometrically non-linear analysis of large deformation.



DOI: 10.1002/nme

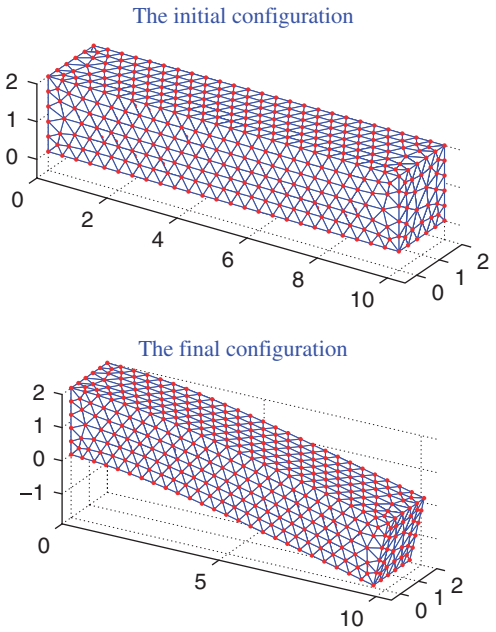


Figure 21. The initial and final configuration of the 3D cantilever beam subjected to a regular distributed load using the FS-FEM in the geometrically non-linear analysis of large deformation.

Table III. Tip deflection (cm) versus the load step of the 3D cantilever beam subjected to a regular distributed load.

| Load step ($n$) | FEM-T4 (linear) (1322 nodes) | FEM-T4 (non-linear) (1322 nodes) | FEM-H8 (non-linear) (1323 nodes) | FS-FEM (non-linear) (1322 nodes) |
|---|---|---|---|---|
| 1 | 0.2364 | 0.2295 (3)* | 0.2421 (3) | 0.2365 (3) |
| 2 | 0.4728 | 0.4314 (3) | 0.4522 (3) | 0.4430 (3) |
| 3 | 0.7092 | 0.6119 (3) | 0.6405 (3) | 0.6277 (3) |
| 4 | 0.9456 | 0.7831 (3) | 0.8205 (3) | 0.8038 (3) |
| 5 | 1.1819 | 0.9511 (3) | 1.0022 (4) | 0.9818 (4) |
| 6 | 1.4183 | 1.1210 (4) | 1.1762 (4) | 1.1516 (4) |
| 7 | 1.6547 | 1.2847 (4) | 1.3495 (4) | 1.3206 (4) |
| 8 | 1.8911 | 1.4479 (4) | 1.5222 (4) | 1.4891 (4) |
| 9 | 2.1275 | 1.6104 (4) | 1.6943 (4) | 1.6569 (4) |
| 10 | 2.3639 | 1.7724 (4) | 1.8656 (4) | 1.8242 (4) |

*The number in the bracket shows the number of iterations.

### *7.4. An axletree base: a geometrically non-linear analysis of large deformation*

In this example, a geometrically non-linear analysis of large deformation of an axletree base is studied using the present FS-FEM. As shown in Figure 23, the axletree base is symmetric about



DOI: 10.1002/nme

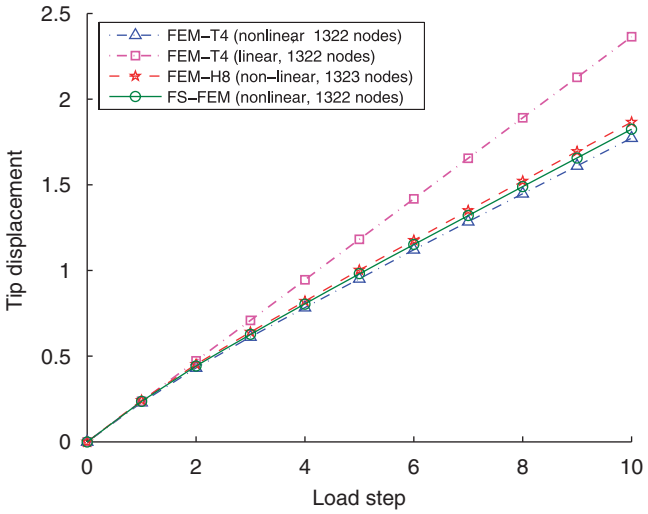


Figure 22. Tip deflection (cm) versus the load step of the 3D cantilever beam subjected to a regular distributed load in the geometrically non-linear analysis of large deformation.

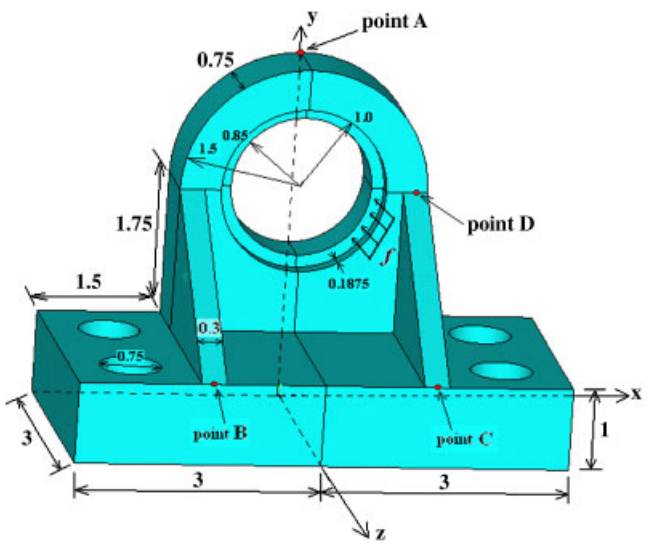


Figure 23. Axletree base model.

the $y$–$z$ plane and discretized using a mesh including 1342 nodes and 5124 tetrahedral elements. The axletree base is subjected to a uniformly distributed force $f$ on the inside circle rim in the $z$-direction and fixed in the locations of four lower cylindrical holes and the bottom plane. The related parameters are taken as $E=3.0\times10^7\,\text{kPa}$, $v=0.3$. The analysis based on the total Lagrange formulation is carried out using 10 increment steps ($n=10$) with $\Delta f=400\,\text{kN/cm}^2$ in each step.



DOI: 10.1002/nme

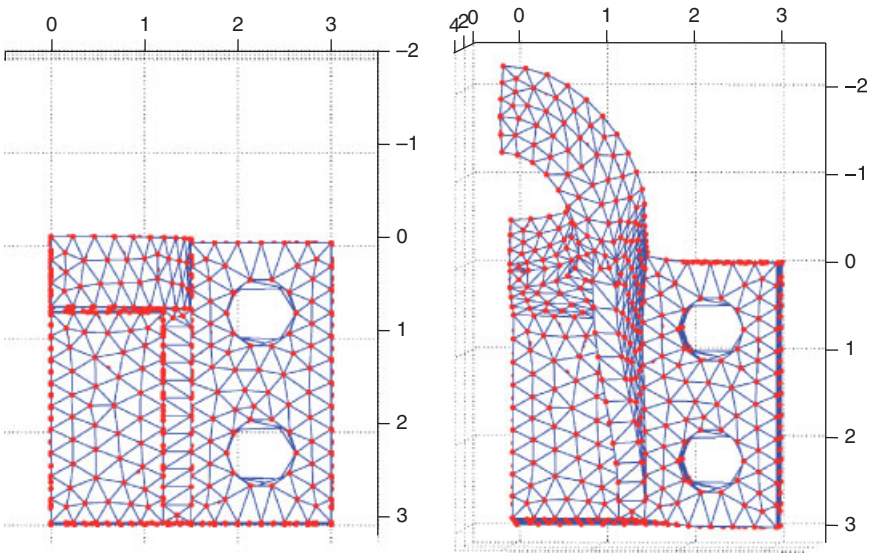


Figure 24. The initial and final configuration viewed from the top of an 3D axletree base using 4-node tetrahedral elements in the geometrically non-linear analysis of large deformation.

Table IV. Tip displacement (point A) in the $z$-direction versus the load step of an 3D axletree base using 4-node tetrahedral elements in the geometrically non-linear analysis of large deformation.

| Load step ($n$) | FEM-T4 (linear) (1342 nodes) | FEM-T4 (non-linear) (1342 nodes) | FEM-T4 (non-linear) (2520 nodes) | FS-FEM (non-linear) (1342 nodes) |
|---|---|---|---|---|
| 1 | 0.3534 | 0.3104 (3)* | 0.3260 (3) | 0.3274 (3) |
| 2 | 0.7068 | 0.5700 (4) | 0.5990 (4) | 0.6017 (4) |
| 3 | 1.0601 | 0.8120 (5) | 0.8538 (5) | 0.8577 (5) |
| 4 | 1.4135 | 1.0419 (5) | 1.0963 (5) | 1.1012 (5) |
| 5 | 1.7669 | 1.2568 (6) | 1.3210 (6) | 1.3268 (6) |
| 6 | 2.1203 | 1.4650 (6) | 1.5393 (6) | 1.5460 (6) |
| 7 | 2.4737 | 1.6652 (7) | 1.7360 (7) | 1.7434 (7) |
| 8 | 2.8271 | 1.8436 (7) | 1.9340 (7) | 1.9421 (7) |
| 9 | 3.1804 | 2.0269 (8) | 2.1074 (8) | 2.1161 (8) |
| 10 | 3.5338 | 2.1855 (8) | 2.2901 (8) | 2.2996 (8) |

*The number in the bracket shows the number of iterations.

Figure 24 displays the initial and final configurations viewed from the top of a 3D axletree base after 10 steps of increment of the deformation using the FS-FEM. Table IV and Figure 25 show the relation between the tip displacement (point A) in the $z$-direction versus the load step of different methods. The simulation converges at a rapid speed and in each load increment, only less than nine times of iteration are performed. It can be seen that the non-linear effects make the



DOI: 10.1002/nme

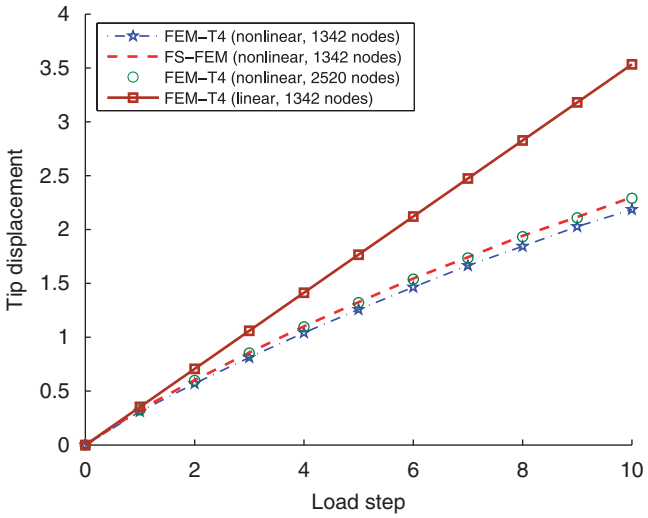


Figure 25. Tip displacement (point A) in the $z$-direction versus the load step of an 3D axletree base using 4-node tetrahedral elements in the geometrically non-linear analysis of large deformation.

axletree base behave stiffer compared with the linear solutions. In the geometrically non-linear analysis, the results of FS-FEM are softer than those of FEM-T4 and almost similar to that of the FEM-T4 using 2520 nodes. Note that for this problem a discretization using 8-node hexahedral elements is impossible due to the complicated geometry of the problem at points B, C or D as shown in Figure 23. All these results again show that the FS-FEM performs more accurately than the FEM-T4 in 3D geometrically non-linear analysis of large deformation.

## 8. CONCLUSIONS

In this work, a FS-FEM is proposed and applied for 3D solid mechanics problems. The FS-FEM uses T4 elements that can be generated automatically for complicated domains. In the FS-FEM, the system stiffness matrix is computed using strains smoothed over the smoothing domains associated with the faces of the tetrahedral elements. Through the formulation and numerical examples, the results demonstrated that the FS-FEM is significantly more accurate than the FEM using tetrahedral elements for both linear analysis and geometrically non-linear analysis of large deformation. In addition, a novel domain-based selective scheme is proposed leading to a combined FS/NS-FEM model that is immune from volumetric locking and hence works well for nearly incompressible materials. The implementation of the FS-FEM is straightforward and no penalty parameters or additional degrees of freedom are used. The computational efficiency of the FS-FEM is found better than that of the FEM-T4 in terms of CPU time for the same accuracy in both strain and displacement error norms.



DOI: 10.1002/nme

REFERENCES


1. Dohrmann CR, Key SW, Heinstein MW, Jung J. A least squares approach for uniform strain triangular and tetrahedral finite elements. *International Journal for Numerical Methods in Engineering* 1998; **42**:1181–1197.
2. Dohrmann CR, Heinstein MW, Jung J, Key SW, Witkowski WR. Node-based uniform strain elements for three-node triangular and four-node tetrahedral meshes. *International Journal for Numerical Methods in Engineering* 2000; **47**:1549–1568.
3. Puso MA, Solberg J. A formulation and analysis of a stabilized nodally integrated tetrahedral. *International Journal for Numerical Methods in Engineering* 2006; **67**:841–867.
4. Liu GR. *Meshfree Methods*: *Moving Beyond the Finite Element Method*. CRC Press: Boca Raton, U.S.A., 2002.
5. Gu YT. Meshfree methods and their comparisons. *International Journal of Computational Methods* 2005; **2**: 477–515.
6. Chen JS, Wu CT, Yoon S, You Y. A stabilized conforming nodal integration for Galerkin meshfree method. *International Journal for Numerical Methods in Engineering* 2000; **50**:435–466.
7. Yoo JW, Moran B, Chen JS. Stabilized conforming nodal integration in the natural-element method. *International Journal for Numerical Methods in Engineering* 2004; **60**:861–890.
8. Liu GR. A generalized gradient smoothing technique and the smoothed bilinear form for Galerkin formulation of a wide class of computational methods. *International Journal of Computational Methods* 2008; **5**:199–236.
9. Liu GR. A weakened weak (W2) form for a unified formulation of compatible and incompatible methods: Part I theory and Part II application to solid mechanics problems. *International Journal for Numerical Methods in Engineering* 2008; revised.
10. Liu GR, Zhang GY, Dai KY, Wang YY, Zhong ZH, Li GY, Han X. A linearly conforming point interpolation method (LC-PIM) for 2D solid mechanics problems. *International Journal of Computational Methods* 2005; **2**(4):645–665.
11. Liu GR, Zhang GY, Wang YY, Huang HT, Zhong ZH, Li GY, Han X. A linearly conforming point interpolation method (LC-PIM) for three-dimensional elasticity problems. *International Journal for Numerical Methods in Engineering* 2007; **72**:1524–1543.
12. Liu GR, Li Y, Dai KY, Luan MT, Xue W. A linearly conforming radial point interpolation method for solid mechanics problems. *International Journal of Computational Methods* 2006; **3**(4):401–428.
13. Liu GR, Dai KY, Nguyen TT. A smoothed finite element method for mechanics problems. *Computational Mechanics* 2007; **39**:859–877.
14. Liu GR, Nguyen TT, Dai KY, Lam KY. Theoretical aspects of the smoothed finite element method (SFEM). *International Journal for Numerical Methods in Engineering* 2007; **71**:902–930.
15. Nguyen-Xuan H, Bordas S, Nguyen-Dang H. Smooth finite element methods: convergence, accuracy and properties. *International Journal for Numerical Methods in Engineering* 2008; **74**:175–208.
16. Liu GR, Nguyen-Thoi T, Nguyen-Xuan H, Lam KY. A node-based smoothed finite element method for upper bound solution to solid problems (NS-FEM). *Computers and Structures* 2008; DOI: 10.1016/j.compstruc.2008.09.003.
17. Dai KY, Liu GR, Nguyen TT. An *n*-sided polygonal smoothed finite element method (*n*SFEM) for solid mechanics. *Finite Elements in Analysis and Design* 2007; **43**:847–860.
18. Nguyen-Xuan H, Rabczuk T, Bordas S, Debongnie JF. A smoothed finite element method for plate analysis. *Computer Methods in Applied Mechanics and Engineering* 2008; **197**:1184–1203.
19. Nguyen-Thanh N, Rabczuk T, Nguyen-Xuan H, Bordas S. A smoothed finite element method for shell analysis. *Computer Methods in Applied Mechanics and Engineering* 2008; DOI: 10.1016/j.cma.2008.05.029.
20. Liu GR, Zhang GY. Upper bound solution to elasticity problems: a unique property of the linearly conforming point interpolation method (LC-PIM). *International Journal for Numerical Methods in Engineering* 2008; **74**:1128–1161.
21. Liu GR, Nguyen-Thoi T, Lam KY. A novel Alpha Finite Element Method ($\alpha$FEM) for exact solution to mechanics problems using triangular and tetrahedral elements. *Computer Methods in Applied Mechanics and Engineering* 2008; **197**:3883–3897.
22. Duarte CA, Kim DJ, Quaresma DM. Arbitrarily smooth generalized finite element approximations. *Computer Methods in Applied Mechanics and Engineering* 2006; **196**:33–56.
23. Liu GR, Nguyen-Thoi T, Lam KY. An edge-based smoothed finite element method (ES-FEM) for static, free and forced vibration analyses of solids. *Journal of Sound and Vibration* 2008; DOI: 10.1016/j.jsv.2008.08.027.
24. Nguyen-Thoi T, Liu GR, Nguyen-Xuan H, Lam KY. An *n*-sided polygonal edge-based smoothed finite element method (nES-FEM) for solid mechanics. *Finite Elements in Analysis and Design* 2008; submitted.
25. Bathe KJ. *Finite Element Procedures*. MIT Press, Prentice-Hall: Cambridge, MA, Englewood Cliffs, NJ, 1996.
26. Liu GR, Quek SS. *The Finite Element Method*: *A Practical Course*. Butterworth Heinemann: Oxford, 2003.

27. Zienkiewicz OC, Taylor RL. *The Finite Element Method* (5th edn). Butterworth Heinemann: Oxford, 2000.
28. Pian THH, Wu CC. *Hybrid and Incompatible Finite Element Methods*. CRC Press: Boca Raton, FL, 2006.
29. Simo JC, Hughes TJR. On the variational foundations of assumed strain methods. *Journal of Applied Mechanics* 1986; **53**:51–54.
30. Reddy JN. *An Introduction to Nonlinear Finite Element Analysis.* Oxford University Press: Oxford, 2004.
31. Hughes TJR. *The Finite Element Method*: *Linear Static and Dynamic Finite Element Analysis*. Prentice-Hall: Englewood Cliffs, NJ, 1987.
32. Puso MA, Chen JS, Zywicz E, Elmer W. Meshfree and finite element nodal integration methods. *International Journal for Numerical Methods in Engineering* 2008; **74**:416–446.
33. Nagashima T. Node-by-node meshless approach and its applications to structural analyses. *International Journal for Numerical Methods in Engineering* 1999; **46**:341–385.
34. Rabczuk T, Belytschko T, Xiao SP. Stable particle methods based on Lagrangian kernels. *Computer Methods in Applied Mechanics and Engineering* 2004; **193**:1035–1063.
35. Nguyen VP, Rabczuk T, Bordas S, Duflot M. Meshless methods: a review and computer implementation aspects. *Mathematics and Computers in Simulation* 2008; DOI: 10.1016/j.matcom.2008.01.003.
36. Timoshenko SP, Goodier JN. *Theory of Elasticity* (3rd edn). McGraw-Hill: New York, 1970.